Acta Crystallographica Section F
Structural Biology and Crystallization Communications
ISSN 1744-3091

A new crystal lattice structure of *Helicobacter pylori* neutrophil-activating protein (HP-NAP)

Osamu Tsuruta, Hideshi Yokoyama* and Satoshi Fujii

School of Pharmaceutical Sciences,
University of Shizuoka, 52-1 Yada, Suruga-ku,
Shizuoka-shi, Shizuoka 422-8526, Japan

Correspondence e-mail:
h-yokoya@u-shizuoka-ken.ac.jp

Received 30 September 2011
Accepted 7 December 2011

PDB References: HP-NAP, apo, 3t9j; iron-loaded, 3ta8.

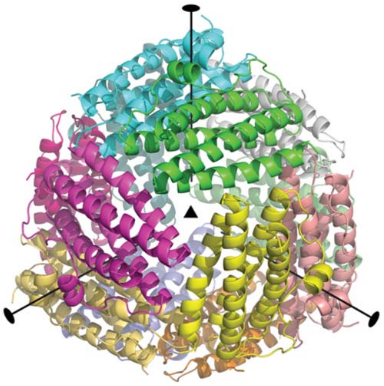

A new crystal lattice structure of *Helicobacter pylori* neutrophil-activating protein (HP-NAP) has been determined in two forms: the native state (Apo) at 2.20 Å resolution and an iron-loaded form (Fe-load) at 2.50 Å resolution. The highly solvated packing of the dodecameric shell is suitable for crystallographic study of the metal ion-uptake pathway. Like other bacterioferritins, HP-NAP forms a spherical dodecamer with 23 symmetry including two kinds of channels. Iron loading causes a series of conformational changes of amino-acid residues (Trp26, Asp52 and Glu56) at the ferroxidase centre.

1. Introduction

Infection of the stomach by *Helicobacter pylori* causes neutrophils to infiltrate the mucosa, which contributes substantially to *H. pylori*-induced gastritis (Warren & Marshall, 1983; Marshall *et al.*, 1985; Goodwin, 1997; Bayerdorffer *et al.*, 1992; Fiocca *et al.*, 1992). *H. pylori* neutrophil-activating protein (HP-NAP), a pathogenic factor, induces neutrophils to adhere to endothelial cells and prompts the production of reactive oxygen intermediates (ROIs; Evans *et al.*, 1995). HP-NAP is localized in the bacterial cytosol and is released upon autolysis. HP-NAP can bind to the external surface of the outer membrane (Namavar *et al.*, 1998).

An amino-acid sequence comparison (Tonello *et al.*, 1999) indicated that HP-NAP belongs to the DNA-protecting protein under starved conditions (Dps) family, which has significant structural similarity to the ferritin family. HP-NAP and Dps protect DNA from oxidative stress; however, HP-NAP only works at low pH and binds DNA molecules differently from Dps (Ceci *et al.*, 2007). HP-NAP forms dodecamers, and electron microscopy has revealed hexagonal rings 9–10 nm in diameter with a hollow central core in which a maximum of 500 Fe atoms per oligomer are capable of binding (Tonello *et al.*, 1999). The X-ray crystal structure of HP-NAP from strain 26695 (HP-NAP 26695) containing one iron ion per monomer has been solved (Zanotti *et al.*, 2002) and the quaternary structure was found to be similar to those of dodecameric bacterial ferritins (Crichton & Declercq, 2010). The dodecamer adopts 23 symmetry and possesses two different threefold pores. The X-ray structure of *Salmonella enterica* Dps has recently been determined in native and iron-soaked forms (Miyamoto *et al.*, 2011). With iron soaking, two chelating residues, Glu82 and Asp78, were rearranged; the other residues involved in iron binding were located at almost the same positions as in the native form.

In this study, the native (Apo) form and an iron-containing (Fe-load) form of HP-NAP from strain YS39 (HP-NAP YS39) were determined. HP-NAP YS39 differs from HP-NAP 26695 at three residues (E46G, V59A and I73L). HP-NAP YS39 was crystallized in a new crystal lattice with space group $F432$ (compared with $P2_1$ for HP-NAP 26695), in which the highly hydrated packing forms a large solvent channel. Structural comparison between the Apo and Fe-load forms indicates similar rearrangements of the iron-binding residues to those in *S. enterica* Dps. An additional pore structure for the influx and efflux of metal ions was clarified.

2. Materials and methods

2.1. Protein expression, purification and crystallization

The expression vector pET15b (Novagen) containing HP-NAP YS39 with *Nde*I and *Bam*HI restriction sites was kindly provided by Professor R. Nozawa, University of Shizuoka, Japan. *Escherichia coli* BL21 (DE3) cells were transformed with the vector. The transformed cells were grown in Luria–Bertani medium containing 0.1 mg ml^{-1} ampicillin at 310 K. When the optical density at 660 nm reached 0.5, isopropyl β-D-1-thiogalactopyranoside was added to a final concentration of 1 m*M* for protein induction. After 6 h, the cells were harvested by centrifugation, resuspended in 50 m*M* Tris–HCl pH 8.8, 0.15 *M* NaCl, 0.1%(*w*/*v*) Nonidet P40 (Roche) and 0.1 *M* L-arginine (Wako) with protease-inhibitor cocktail (Roche) and DNase I (Sigma) and disrupted by sonication. After centrifugation to remove cell debris, the target protein was isolated by nickel-affinity column chromatography. L-Arginine was added to the eluate to a final concentration of 0.1 *M* (Tsumoto *et al.*, 2004). The eluate was applied onto a PD-10 (GE Healthcare) desalting column equilibrated with 50 m*M* Tris–HCl pH 7.5 containing 0.1 *M* L-arginine with a final pH of 8.8. The collected solution was concentrated using a Vivaspin-20 centrifugal concentrator (Sartorius) with a 10 kDa molecular-mass cutoff.

Crystallization was performed using the hanging-drop vapourdiffusion method at 293 K. Crystallization drops were prepared by mixing 1 µl protein solution (10 mg ml^{-1}) and 1 µl reservoir solution consisting of 20%(*v*/*v*) ethylene glycol; Apo crystals were obtained in three weeks. To obtain Fe-load crystals, a reservoir solution consisting of 20%(*v*/*v*) ethylene glycol and 10 m*M* iron(II) sulfate was used. Cubic or rectangular-shaped crystals appeared and their typical dimensions were 0.2 × 0.2 × 0.2 mm.

2.2. Data collection and processing

X-ray data collection was performed on beamlines BL5A and NE3A at the KEK Photon Factory (Tsukuba, Japan). For cryoprotection, crystals were rapidly transferred into a solution consisting of 30%(*v*/*v*) glycerol in the mother liquor and were flash-frozen in a stream of N_2 at 95 K just prior to collection of the X-ray diffraction data. The X-ray wavelength was set to 1.0000 Å for the Apo crystal and 1.5000 Å for the Fe-load crystal. To obtain anomalous dispersion signals from the bound Fe atoms, a data set to 1.7185 Å resolution was also collected from the Fe-load crystal. The diffraction images were scaled using the *HKL*-2000 package (Otwinowski & Minor, 1997).

2.3. Structure determination and refinement

The crystal structures were determined by the molecular-replacement method using *MOLREP* (Vagin & Teplyakov, 2010) as implemented in the *CCP*4 suite (Winn *et al.*, 2011) with chain *A* of HP-NAP 26695 (PDB entry 1ji4; Zanotti *et al.*, 2002) as the search model. Crystallographic refinements were made with *REFMAC*5 (Murshudov *et al.*, 2011) as implemented in the *CCP*4 suite. Model building and structural adjustments were performed using *Coot* (Emsley & Cowtan, 2004). All molecular figures were prepared with *PyMOL* (DeLano, 2002). The statistics of X-ray data collection and crystallographic refinement are summarized in Table 1.

After refinement, an anomalous difference map was calculated using the data collected at 1.7185 Å from the Fe-load crystal. Two notable anomalous difference peaks were observed at the known ferroxidase centre and the centre of pore I (Fig. 1). The peak heights were 21.0σ and 6.1σ, respectively.

Table 1
Diffraction data and refinement statistics.

Values in parentheses are for the highest resolution shell.

	Apo	Fe-load	
Crystal parameters			
Space group	*F*432	*F*432	
Unit-cell parameter (Å)	a = 189.47	a = 188.53	
Solvent content (%)	67.06	66.57	
Matthews coefficient (Å^3 Da^{-1})	3.73	3.68	
No. of molecules in asymmetric unit	1	1	
Data collection			
X-ray wavelength (Å)	1.0000	1.5000	1.7185
Resolution (Å)	20–2.2 (2.59–2.20)	50–2.5 (2.59–2.50)	50–2.55 (2.64–2.55)
$\langle I/\sigma(I)\rangle$	66.4 (11.2)	39.7 (4.93)	33.4 (4.76)
No. of observed reflections	206987	140468	130986
No. of unique reflections	15374	10445	9826
Completeness (%)	99.9 (100.0)	99.9 (99.7)	100.0 (100.0)
Multiplicity	13.76	13.44	13.33
$R_{\rm merge}$†	0.064 (0.248)	0.076 (0.393)	0.092 (0.378)
Refinement			
No. of used reflections	14456	9898	
$R_{\rm work}/R_{\rm free}$‡§	0.223/0.248	0.212/0.242	
Temperature factor (Å^2)	36.0	41.6	
Model composition (per subunit)			
No. of non-H atoms	1287	1276	
No. of amino acids	144	144	
No. of iron ions	0	2	
No. of water molecules	96	71	
No. of ligand atoms	4	16	
Geometry			
R.m.s.d. bond lengths (Å)	0.006	0.013	
R.m.s.d. bond angles (°)	0.865	1.365	
Ramachandran plot, residues in			
Favoured region (%)	98.5	96.4	
Allowed region (%)	1.5	3.6	
Outlier region (%)	0.0	0.0	

† $R_{\rm merge} = \sum_{hkl}\sum_i |I_i(hkl) - \langle I(hkl)\rangle| / \sum_{hkl}\sum_i I_i(hkl)$, where $I_i(hkl)$ and $\langle I(hkl)\rangle$ are the measured and averaged intensities of multiple measurements of the same reflection, respectively. ‡ $R_{\rm work} = \sum_{hkl}\big||F_{\rm obs}| - |F_{\rm calc}|\big| / \sum_{hkl}|F_{\rm obs}|$, where $F_{\rm obs}$ and $F_{\rm calc}$ are the observed and calculated structure-factor amplitudes, respectively, for 95% of the reflection data used in the refinement. § $R_{\rm free} = \sum_{hkl}\big||F_{\rm obs}| - |F_{\rm calc}|\big| / \sum_{hkl}|F_{\rm obs}|$ for 5% of the reflection data that were excluded during refinement.

The atomic coordinates and structure factors of the Apo and Fe-load forms have been deposited in the PDB under accession codes 3t9j and 3ta8, respectively.

3. Results and discussion

3.1. Heavily solvated crystal lattice

HP-NAP YS39 was crystallized in a new crystalline lattice belonging to the cubic space group *F*432 with one protomer in the asymmetric unit. In the crystal, 12 protomers form a dodecamer like a spherical vesicle about 90 Å in diameter with crystallographic point group 23. One dodecamer makes crystal contacts with six neighbouring dodecamers, giving a simple cubic packing with a crystallographic fourfold axis as shown in Fig. 2(*a*).

Inter-dodecamer contacts are made through the central regions of helices 2–3 of four protomers. As shown in Fig. 2(*b*), there are four bridged stacks of Lys74 residues, in which each terminal ε-amino group forms strong hydrogen bonds to three backbone carbonyl O atoms. The hydrogen-bond distances between Lys74 N$^{\varepsilon}$ and Thr76 O, Lys74 O and Ile73 O are 2.6, 2.8 and 2.8 Å, respectively (Fig. 2*c*). The bridged stacks are stabilized by hydrophobic interactions with the neighbouring alkyl side chains.

This new packing system forms a large three-dimensional rectangular solvent channel across the crystal. In the crystal, a dodecamer adopts a hollow core and forms eight pores on both surface sides of the four threefold axes. A spherical shell-like dodecameric assembly forms crystal contacts with six neighbouring dodecamers, giving a face-centred cubic packing (space group *F*432) which contrasts with the characteristic pseudo-hexagonal sheet packing of the HP-NAP 26695 crystal structure (PDB entry 1ji4). Owing to the lysine stacks, the distance between the centres of the adjacent spherical dodecamers is ~5 Å longer than that in HP-NAP 26695 and therefore the heavily solvated crystal lattice forms a wide water channel. The solvent content and $V_{\rm M}$ are 65%(*v*/*v*) and 3.68 Å^3 Da^{-1}, respectively, whereas those of the HP-NAP 26695 crystal are 55%(*v*/*v*) and 2.78 Å^3 Da^{-1}, respectively.

There is no masking contact with the adjacent dodecamers at the pores along the threefold axis, which prevents metal ions flowing in and/or out (Fig. 2*a*). The two different pores along the threefold axis are a notable feature as they are open to solvent channels. This three-directional system of canals might be useful in metal-soaking studies.

3.2. Overall structure of HP-NAP

The monomer of HP-NAP is composed of a four-helix bundle (helices 1, 2, 3 and 4, in sequence) with a fifth helix (helix 2–3) of seven residues (Leu69–Leu75) oriented almost perpendicular to the bundle. Superposition of the C$^\alpha$ atoms of monomers of the HP-NAP YS39 (Fe-load) and HP-NAP 26695 structures yields a root-mean-square (r.m.s.) deviation of 0.36 Å. Although the two structures belong to different space groups (*F*432 for HP-NAP YS39 and *P*2$_1$ for HP-NAP 26695), the structures of the monomers are very similar to each other.

Superposition of equivalent C$^\alpha$ atoms of the HP-NAP monomer in the Apo and Fe-load structures yields an r.m.s. deviation of 0.54 Å. Significant differences are observed in the metal-coordinating residues at the ferroxidase centre and Phe34 at pore II (described below). In the Apo structure the internal cavity is likely to be filled with disordered solvent molecules, and no metal ion such as magnesium was detected. However, one ethylene glycol molecule per asymmetric unit is located in the hydrophobic groove between the helices which form the inner surface of the shell. In the Fe-load structure two additional ethylene glycol molecules are observed at the interface of the helices.

3.3. The ferroxidase centre

Two ferroxidase centres are located between two antiparallel subunits related by a twofold axis (Fig. 3*a*). In the Fe-load structure, a ferric iron (Fe1) located at one ferroxidase site is 21.6 Å from Fe1 at another symmetry-related ferroxidase site. This value is almost the same as that for the recurrent inter-ferroxidase site reported in the Dps family (Ren *et al.*, 2003). The ligands of Fe1 are provided by two different subunits: His25, located on helix 1 of one subunit, and Asp52 and Glu56, located on helix 2 of the other subunit. Superposition of the equivalent C$^\alpha$ atoms of the dimeric *α*-helix bundles (helices 1, 2, 3 and 4) between the Apo and Fe-load structures yields an r.m.s. deviation of 0.92 Å. This indicates that the shift and orientational changes of the helices containing the metal-binding residues occur by chelation.

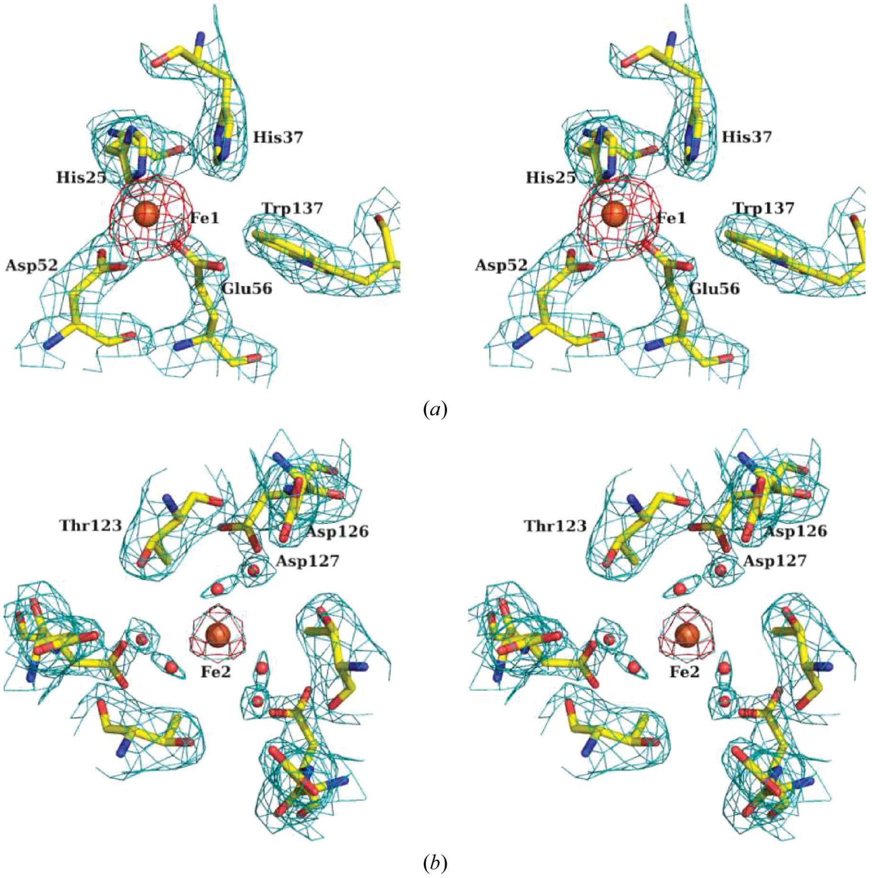

Figure 1
Stereo representations of the electron densities at two iron-binding sites. $2F_{\rm o} - F_{\rm c}$ maps are coloured light blue and contoured at 1.2*σ*. The anomalous difference maps at 3.0*σ* around iron ions are coloured red. Fe atoms and water molecules are shown as brown and red spheres and neighbouring residues are shown as stick models. (*a*) The ferroxidase centre at the dimer interface. (*b*) Pore I viewed from above along the threefold axis.

All ferroxidase centres so far described contain di-iron sites, with the two ions separated by a distance of about 3 Å. In HP-NAP 26695 the first iron ion was observed and the second ion was an unidentified solvent atom (Zanotti *et al.*, 2002). In HP-NAP YS39 no ion or solvent atom was observed at the second ion position (Fig. 1*a*).

Several conformational changes were also observed at the positions of key residues, Asp52 and Glu56, that are involved in chelation. The positions of the carboxyl groups differed by 3.1 Å for Asp52 C^{γ} and by 3.4 Å for Glu56 C^{δ} between the two structures. Moreover, the superposition revealed the C^{α} displacements of helix 2 to be significantly larger than those of other helices; the r.m.s.d.s of helices 1, 2, 3 and 4 were 0.61, 1.29, 0.90 and 0.65 Å, respectively. Helix 2 possesses two major residues involved in iron binding and its displacement might allosterically promote binding of the other iron by the same dimer. Upon binding an iron in the ferroxidase centre, Trp26 switches by ~180° between two rotameric conformations (χ_2; Fig. 3*b*). The carboxyl group of Glu56 and Fe1 in the Fe-load structure in fact overlap partially at the position of the aromatic side chain of Trp26 in the Apo structure (shown in Fig. 3*b*). Once the aromatic side chain of Trp26 flips out of the ferroxidase site, the carboxyl O atoms of Asp52 and Glu56 can be chelated by iron. In the Apo structure the orientation of Asp52 ($O^{\delta1}$) is stabilized by a salt bridge to His22 ($N^{\varepsilon2}$) at 2.86 Å through a rotational conformational change (Asp52 χ_1). The position of Glu56 is also stabilized by a water-mediated hydrogen bond to Lys134 through a rotational change (Glu56 χ_1). Iron loading disrupts the salt bridges between Asp52 and His22 and between Glu56 and Lys134 to the benefit of iron chelation.

His25, His37 and Tyr44 situated close to Fe1 do not differ significantly in the two structures. Phe33, which adopts close stacking with His37, also maintains the same position. Trp26 is well conserved among HP-NAP-like proteins and occurs at the interface of the twofold-related subunits; therefore, the change in the orientation of Trp26 located in the vicinity of the ferroxidase centre might play an important role in switching the iron binding and/or regulating the ferroxidase activity.

3.4. Pore I

The dodecamer possesses four threefold axes, each of which in passing through the shell in two different threefold environments is arranged as pores on the surface of a sphere. One of the two threefold pores corresponds to pore I, which has a strongly hydrophilic and negatively charged environment. Pore I has three sets of filters for metal ions. The filters are formed by the rigid loop region (Glu114) located around the N-terminus of helix 4 and successive residues (Asp126 and Asp127) located in the middle of helix 4. These arrangements around threefold rotational axes form a funnel-like shape through which metal ions are efficiently passed by electrostatic interaction (shown in Fig. 4).

This kind of pore is present in Dps (defined as the channel at the N-terminal threefold axis), *Listeria innocua* ferritin, *Bacillus anthracis* Dlp-1, *Salmonella enterica* Dps and *Deinococcus radiodurans* Dps2 (Ilari *et al.*, 2000; Papinutto *et al.*, 2002; Miyamoto *et al.*, 2011; Cuypers *et al.*, 2007). In the Apo structure this channel is filled

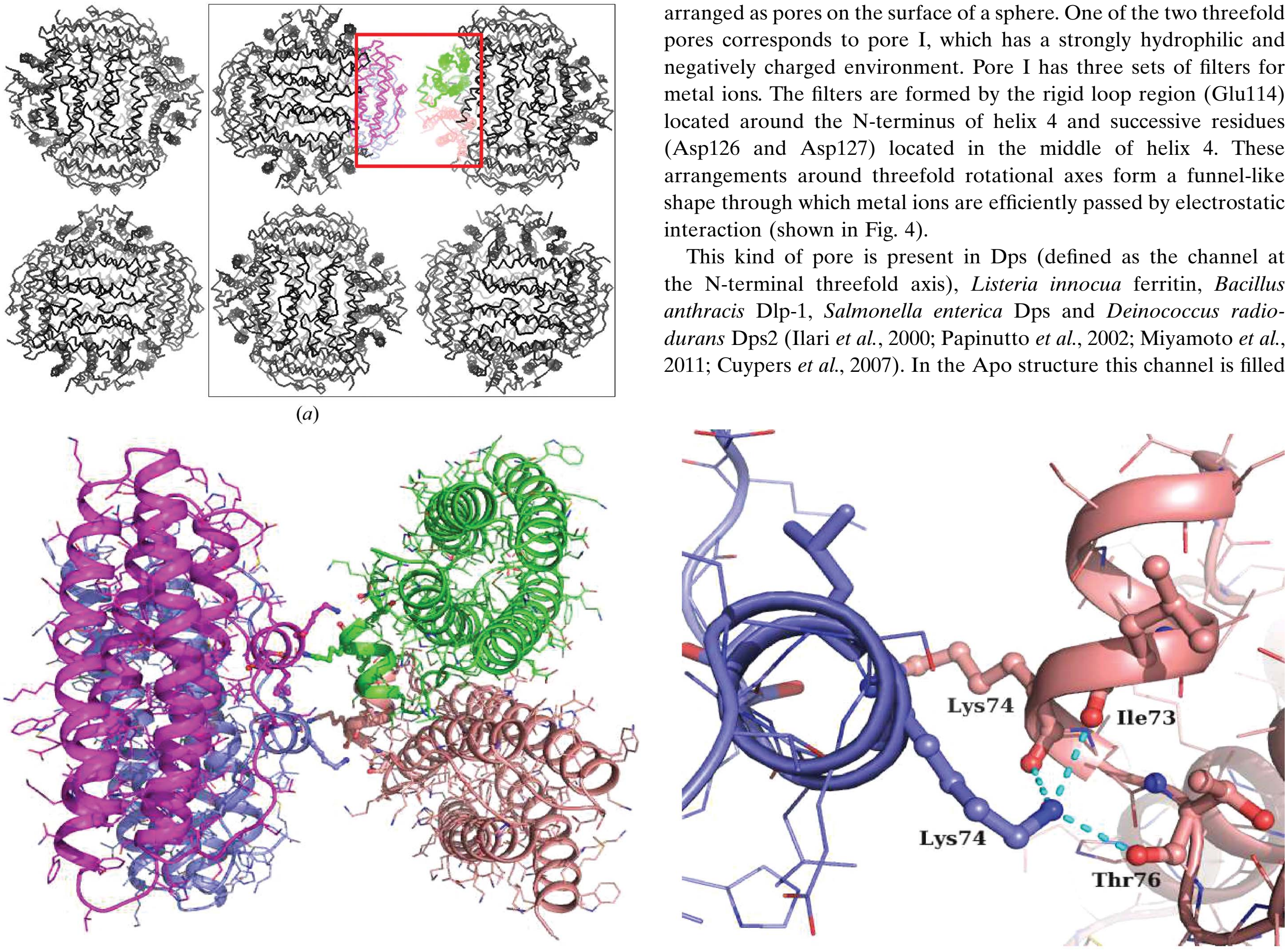

(*a*)

(*b*)

(*c*)

Figure 2
Crystal structure of HP-NAP YS39 in the new crystal packing (space group *F*432). Inter-dodecamer contacts are made through the bridged stacks of Lys74 residues. Each terminal ε-amino group of the four bridged stacks of Lys74 residues forms strong hydrogen bonds to the three backbone carbonyl O atoms. (*a*) Representative dodecamers are shown in a cubic lattice in a projection along the *a* axis. An unit cell is shown as thin lines. The four protomers shown in (*b*) are presented in different colours. (*b*) A close-up view of the molecular contacts between two neighbouring dodecamers. Each protomer is shown in the same colour as in (*a*). The key residues Lys74, Ile73 and Thr76 are presented as ball-and-stick models. (*c*) A close-up view of Lys74 stacks between the dodecamers. The bridged stacks are built with strong hydrogen bonds between the terminal ε-amino group of Lys74 and the three backbone carbonyl O atoms. These hydrogen bonds are indicated by cyan dashed lines.

with a network of solvent molecules and is a possible path for the entry of iron ions into the internal cavity. However, no significant solvent water molecule was observed on the inner side of the pore in the Fe-load structure. In the Fe-load structure the doped iron is

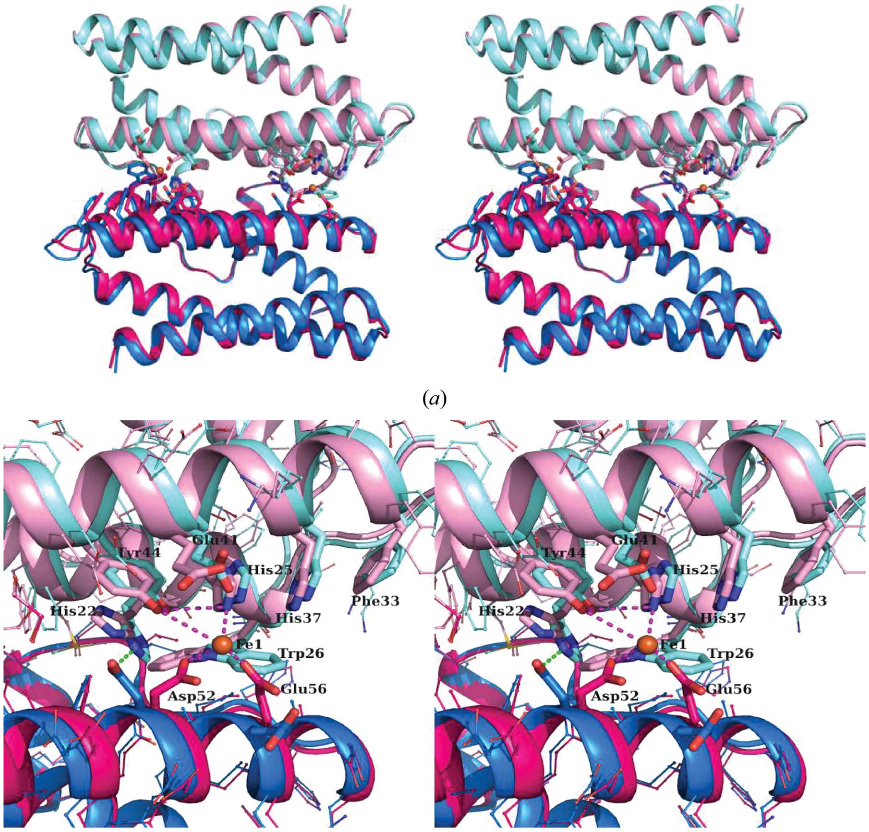
(*a*)

(*b*)

Figure 3
Comparative views of the ferroxidase centre. Two ferroxidase centres are built from two antiparallel subunits related by the twofold rotational axis. On Fe loading, several structural changes are observed at the ferroxidase centre. The superposition of the equivalent C$^{\alpha}$ atoms of the dimeric α-helical bundles was calculated. (*a*) Stereoview of the superposition of the Apo (blue and cyan) and Fe-load (red and pink) structures. The key residues at ferroxidase centres, Trp26, Asp52 and Glu56, are presented as stick models and the Fe atoms observed in the Fe-load structure are shown as brown spheres. The superposition reveals that helix 2 at the interface of the dimer is significantly displaced by Fe-loading. (*b*) A close-up stereoview of one ferroxidase centre. The residues and Fe atom are coloured as in (*a*). Several conformational changes involved in the chelation are observed at Trp26, Asp52 and Glu56, which are shown as thick sticks. Residues around the chelation site, His22, His25, Phe33, His37, Glu41 and Tyr44, are also presented as thick sticks. Magenta dashed lines show the hydrogen bonds observed in the Fe-load structure and a green dashed line indicates the salt bridge between His22 and Asp52 in the Apo structure.

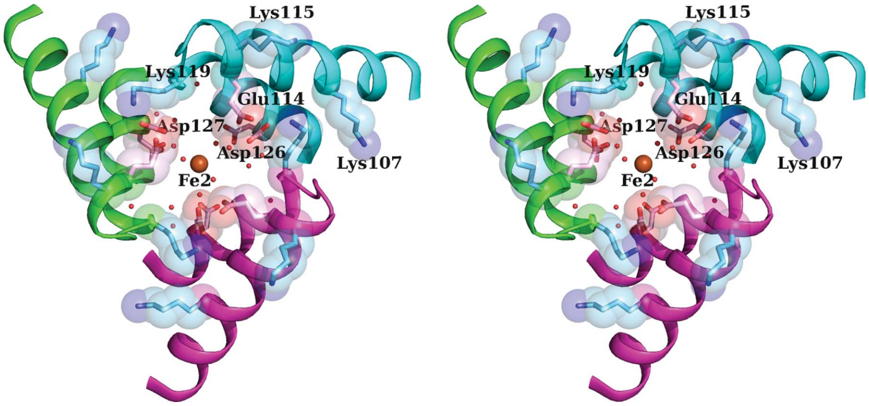

Figure 4
Stereoview of pore I. The trimeric pore is viewed from above along the threefold axis (from outside the spherical shell). Pore I with a funnel-like shape is built from a threefold-related trimer and the filters of the pore are formed by the rigid loop region (Glu114) and successive helical residues (Asp126 and Asp127). Three polypeptide chains are shown as cyan, green and magenta ribbon models and the key residues and Fe atom are represented by space-filling and stick models and by a brown sphere, respectively. Acidic and basic moieties of key residues are represented by space-filling models coloured pink and light blue, respectively. The positively charged lysine residues (Lys107, Lys115 and Lys119) are also shown as stick models.

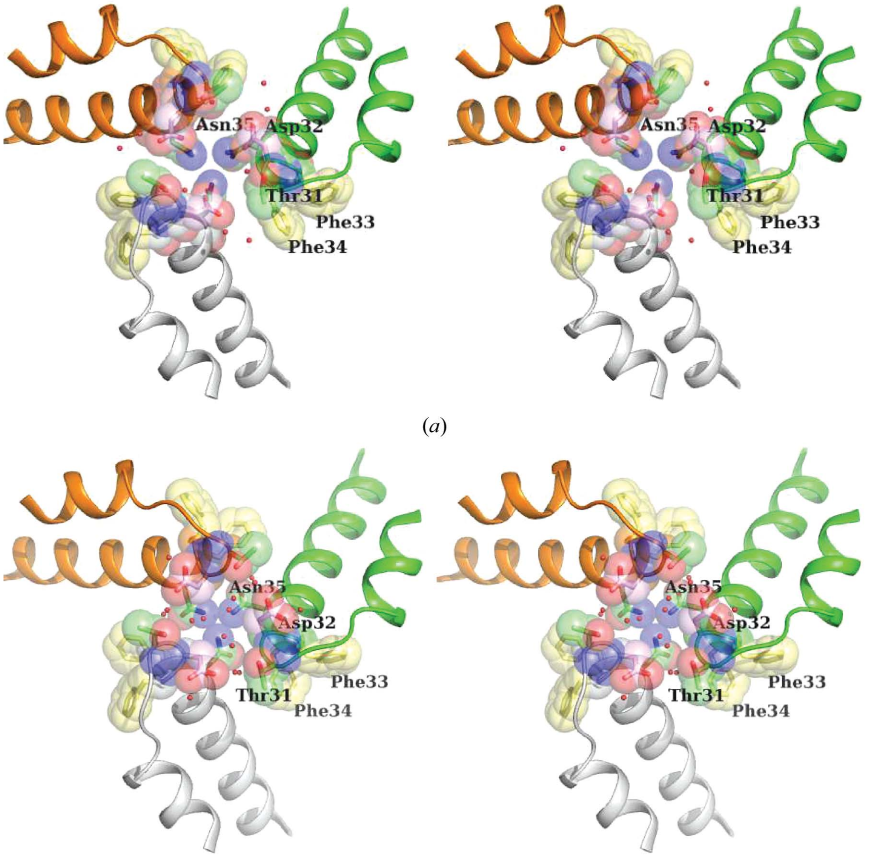

(*a*)

(*b*)

Figure 5
Stereoview of pore II. The trimeric pore is viewed from above along the threefold axis (from outside the spherical shell). Pore II is built from a threefold-related trimer and the filters of the pore are formed by hydrophilic and polar residues (Thr31, Asp32 and Asn35). The three polypeptide chains are represented by grey, green and orange ribbon models and the key residues by space-filling and stick models. The hydrophobic residues (Phe33 and Phe34) on the inner side of the pore are also shown as stick models. Acidic, basic, hydrophobic and hydrophilic moieties of key residues are presented as space-filling models coloured pink, light blue, light green, and light yellow, respectively. The water molecules observed in the Fe-load structure are also shown as red spheres. (*a*) Apo structure. (*b*) Fe-load structure.

located at the centre of three Asp127 residues (Fe2). Because of the disordered electron density owing to the high-symmetry space group, suitable ligands are not clearly evident.

The distance between Fe2 and Asp127 $O^{\delta1}$ is 4.05 Å, indicating that the disordered water molecule chelated to an iron ion is connected to $O^{\delta1}$ through the hydrogen-bond network. Such a flexible rearrangement might be compatible with the trapping of a metal ion and might transfer an iron to the ferroxidase centre. The positively charged environment, with three lysine residues (Lys107, Lys115 and Lys119), around this negatively charged pore provides an effective electrostatic potential for metal-ion transfer. Lys115 is located close to the negatively charged pore filter and is also positioned outside the entrance to the channel (shown in Fig. 4). A highly disordered structure around the threefold axis could not elucidate the hydrogen-bond systems with these carboxyl groups of Asp and Glu robustly and might be suitable for the metal-ion pathway. The inter-subunit distances between the two corresponding carboxyl O atoms of Asp127 of three promoters are 7.01 and 8.06 Å. These pore sizes correspond to the size of the hydrated metal-ion path.

3.5. Pore II

Another kind of threefold pore, pore II, which has two sets of filters, is formed by the rigid loop region (Thr31 and Asp32) and the N-terminal residue Asn35 of helix 2. Asp32 and Thr31, which are located at the entrance to the funnel, are shown in Fig. 5. In the Apo structure the pore-size distances of these filters are 6.2 Å for Asp32 $O^{\delta1}$–Asp32 $O^{\delta1}$* (where the asterisk indicates a residue from another protomer) and 9.3 Å for Thr31 $O^{\gamma1}$–Thr31 $O^{\gamma1}$*; the entry site of pore II might offer an open channel to the narrow solvent region. Three Asn35 residues traverse the threefold rotational axis inside the shell. The pore-size distances of these filters are 3.6 Å for Asn35 $N^{\delta2}$–Asn35 $N^{\delta2}$* and 4.2 Å for Asn35 $O^{\delta1}$–Asn35 $O^{\delta1}$* in the Apo structure; these pore-size distances between Asn35 residues are not suitable for ion selection and control of the amount of ion influx. The inter-subunit distances between the filter atoms, 3.6 and 4.2 Å, are longer than the typical hydrogen-bond distance; these distances are 3.0 and 6.1 Å in the Fe-load structure, respectively. The orientation of the Asn35 carboxyamide in the Apo and Fe-load structures differs as shown in Fig. 5. The bulky side chain of Phe34 makes close contact to Phe33 through a CH–π interaction. This Phe34, which is close to Asn35 in HP-NAP 26695, moves away from Asn35 in HP-NAP YS39. These flexible structures are observed around the inner filter of pore II.

We thank Professor R. Nozawa (University of Shizuoka, Japan) for kindly providing us with the expression vector pET15b containing HP-NAP YS39. We thank the Photon Factory staff for assistance with data collection. This work was supported in part by a Grant-in-Aid for Scientific Research (C) (No. 22590039) to SF from the Japan

Society for the Promotion of Science and also by a Grant-in-Aid for Young Scientists (B) (No. 21770122) to HY from the Ministry of Education, Culture, Sports, Science and Technology in Japan.

References

Bayerdörffer, E., Lehn, N., Hatz, R., Mannes, G. A., Oertel, H., Sauerbruch, T. & Stolte, M. (1992). *Gastroenterology*, **102**, 1575–1582.

Ceci, P., Mangiarotti, L., Rivetti, C. & Chiancone, E. (2007). *Nucleic Acids Res.* **35**, 2247–2256.

Crichton, R. R. & Declercq, J. P. (2010). *Biochim. Biophys. Acta*, **1800**, 705–718.

Cuypers, M. G., Mitchell, E. P., Romão, C. V. & McSweeney, S. M. (2007). *J. Mol. Biol.* **371**, 787–799.

DeLano, W. L. (2002). *PyMOL*. http://www.pymol.org.

Emsley, P. & Cowtan, K. (2004). *Acta Cryst.* D**60**, 2126–2132.

Evans, D. J., Evans, D. G., Takemura, T., Nakano, H., Lampert, H. C., Graham, D. Y., Granger, D. N. & Kvietys, P. R. (1995). *Infect. Immun.* **63**, 2213–2220.

Fiocca, R., Villani, L., Luinetti, O., Gianatti, A., Perego, M., Alvisi, C., Turpini, F. & Solcia, E. (1992). *Virchows Arch. A Pathol. Anat. Histopathol.* **420**, 489–498.

Goodwin, C. S. (1997). *Clin. Infect. Dis.* **25**, 1017–1019.

Ilari, A., Stefanini, S., Chiancone, E. & Tsernoglou, D. (2000). *Nature. Struct. Biol.* **7**, 38–43.

Marshall, B. J., Armstrong, J. A., McGechie, D. B. & Glancy, R. J. (1985). *Med. J. Aust.* **142**, 436–439.

Miyamoto, T., Asahina, Y., Miyazaki, S., Shimizu, H., Ohto, U., Noguchi, S. & Satow, Y. (2011). *Acta Cryst.* F**67**, 17–22.

Murshudov, G. N., Skubák, P., Lebedev, A. A., Pannu, N. S., Steiner, R. A., Nicholls, R. A., Winn, M. D., Long, F. & Vagin, A. A. (2011). *Acta Cryst.* D**67**, 355–367.

Namavar, F., Sparrius, M., Veerman, E. C., Appelmelk, B. J. & Vandenbroucke-Grauls, C. M. (1998). *Infect. Immun.* **66**, 444–447.

Otwinowski, Z. & Minor, W. (1997). *Methods Enzymol.* **276**, 307–326.

Papinutto, E., Dundon, W. G., Pitulis, N., Battistutta, R., Montecucco, C. & Zanotti, G. (2002). *J. Biol. Chem.* **277**, 15093–15098.

Ren, B., Tibbelin, G., Kajino, T., Asami, O. & Ladenstein, R. (2003). *J. Mol. Biol.* **329**, 467–477.

Tonello, F., Dundon, W. G., Satin, B., Molinari, M., Tognon, G., Grandi, G., Del Giudice, G., Rappuoli, R. & Montecucco, C. (1999). *Mol. Microbiol.* **34**, 238–246.

Tsumoto, K., Umetsu, M., Kumagai, I., Ejima, D., Philo, J. S. & Arakawa, T. (2004). *Biotechnol. Prog.* **20**, 1301–1308.

Vagin, A. & Teplyakov, A. (2010). *Acta Cryst.* D**66**, 22–25.

Warren, J. D. & Marshall, B. J. (1983). *Lancet*, **1**, 1273–1275.

Winn, M. D. *et al.* (2011). *Acta Cryst.* D**67**, 235–242.

Zanotti, G., Papinutto, E., Dundon, W., Battistutta, R., Seveso, M., Giudice, G., Rappuoli, R. & Montecucco, C. (2002). *J. Mol. Biol.* **323**, 125–130.